nature photonics

SUPPLEMENTARY INFORMATION

https://doi.org/10.1038/s41566-018-0297-y

In the format provided by the authors and unedited.

Symmetry-breaking-induced nonlinear optics at a microcavity surface

Xueyue Zhang[1,2,7,8], Qi-Tao Cao[1,3,8], Zhuo Wang[4], Yu-xi Liu[2,5], Cheng-Wei Qiu[4], Lan Yang[6], Qihuang Gong[1,3] and Yun-Feng Xiao[1,3]*

[1]State Key Laboratory for Mesoscopic Physics and Collaborative Innovation Center of Quantum Matter, School of Physics, Peking University, Beijing, People's Republic of China. [2]Department of microelectronics and nanoelectronics, Tsinghua University, Beijing, People's Republic of China. [3]Collaborative Innovation Center of Extreme Optics, Shanxi University, Shanxi, People's Republic of China. [4]Department of Electrical and Computer Engineering, National University of Singapore, Singapore, Singapore. [5]Institute of Microelectronics, Tsinghua University, Beijing, People's Republic of China. [6]Department of Electrical and Systems Engineering, Washington University in St. Louis, St. Louis, MO, USA. [7]Present address: Thomas J. Watson, Sr., Laboratory of Applied Physics, California Institute of Technology, Pasadena, CA, USA. [8]These authors contributed equally: Xueyue Zhang, Qi-Tao Cao. *e-mail: yfxiao@pku.edu.cn

Supplementary Information to
Symmetry-breaking-induced nonlinear optics at a microcavity surface

Xueyue Zhang[1,2*], Qi-Tao Cao[1,3*], Zhuo Wang[4], Yu-xi Liu[2,5],
Cheng-Wei Qiu[4], Lan Yang[6], Qihuang Gong[1,3], Yun-Feng Xiao[1,3†]
[1]State Key Laboratory for Mesoscopic Physics and Collaborative Innovation Center of Quantum Matter, School of Physics, Peking University, Beijing 100871, People's Republic of China
[2]Department of microelectronics and nanoelectronics, Tsinghua University, Beijing 100084, People's Republic of China
[3]Collaborative Innovation Center of Extreme Optics, Shanxi University, Shanxi 030006, People's Republic of China
[4]Department of Electrical and Computer Engineering, National University of Singapore, Singapore 117583, Singapore
[5]Institute of Microelectronics, Tsinghua University, Beijing 100084, People's Republic of China
[6]Department of Electrical and Systems Engineering, Washington University in St. Louis, St. Louis, MO 63130, USA.
* These authors contributed equally.
† E-mail: yfxiao@pku.edu.cn

This Supplementary Text is organized as follows. In Section I, we summarize the theoretical model, including the nonlinear coupling between the pump and the second harmonic (SH) modes, coupled mode equations, dynamic phase-matching method assisted by thermal and optical Kerr effects. In Section II, the dependence of the second-harmonic power on the pump power is discussed. In Section III, we present the symmetry-breaking-induced nonlinear effect at the cavity surface and the multipole nonlinear responses in the bulk under different pump polarizations, and show the details of identifying their contributions.

I. THEORETICAL MODEL

A. Nonlinear coupling between the pump mode and the SH mode

For a spherical microcavity with a radius of R, a three-layer model (Supplementary Figure S1) is used to describe the surface optical nonlinear effects within an atomically thin intermediate layer. It is assumed that the refraction index and nonlinear susceptibility should vary sharply across the surface from $r = R^-$ to $r = R^+$ in Supplementary Figure S1, where R^- (R^+) stands for the internal (outside) surface of the thin intermediate layer, and r is the radial position. We consider that only the silica microsphere and the interface region (*i.e.*, $r \in [0,R^+)$) are nonlinear.

The second-harmonic generation (SHG) in such a system can originate from both surface electric-dipole and the bulk electric-multipole responses. The total second-order nonlinear electric polarization $\mathbf{P}^{(2)}$ can be expressed in the form [1, 2]

$$\mathbf{P}^{(2)} = \overleftrightarrow{\chi}^{(2)}_{\mathrm{d}} : \mathbf{E}_1\mathbf{E}_1 + 2\overleftrightarrow{\chi}^{(2)}_{\mathrm{q}} : \nabla\mathbf{E}_1\mathbf{E}_1 - \nabla\cdot(\overleftrightarrow{\chi}^{(2)}_{\mathrm{Q}} : \mathbf{E}_1\mathbf{E}_1), \tag{S1}$$

where $\mathbf{E}_1$ is the pump electric field, the three-order tensor $\overleftrightarrow{\chi}^{(2)}_{\mathrm{d}}$ is the electric-dipole (ED) susceptibility, and the four-order tensor $\overleftrightarrow{\chi}^{(2)}_{\mathrm{q}}$ ($\overleftrightarrow{\chi}^{(2)}_{\mathrm{Q}}$) is the electric-quadrupole (EQ) susceptibility. In particular, $\overleftrightarrow{\chi}^{(2)}_{\mathrm{d}} = \overleftrightarrow{\chi}^{(2)}_{\mathrm{sd}}\delta(r-R)$ for a silica microsphere, with $\delta(r)$ being Dirac delta function and $\overleftrightarrow{\chi}^{(2)}_{\mathrm{sd}}$ being the surface electric-dipole susceptibility tensor, since the centrosymmetry of silica forbids the electric-dipolar nonlinearity in bulk. The Helmholtz equation for the SH electric field $\mathbf{E}_2$ is written as

$$(\nabla^2 - \frac{n_2^2}{c^2}\frac{\partial^2}{\partial t^2})\mathbf{E}_2 = \frac{1}{c^2}\frac{\partial^2\mathbf{P}^{(2)}}{\partial t^2}, \tag{S2}$$

where n_2 is the refractive index in the cavity for SH and c is the speed of light in vacuum.

The electric field $\mathbf{E}_j$ ($j = 1, 2$ for pump and SH, respectively) in a microcavity exhibits the form of $\mathbf{E}_j(\mathbf{x},t) = \tilde{\alpha}_j(t)\mathbf{E}_{0j}(\mathbf{x})e^{-i\omega_j t}$, where $\tilde{\alpha}_j(t)$ is the slowly varying field amplitude and $|\tilde{\alpha}_j(t)|^2$ corresponds to the intracavity energy; $\mathbf{E}_{0j}(\mathbf{x})$ represents the normalized spatial field distribution, ω_j is the frequency of the electric field. Here, the wave vectors of both the pump and SH modes are along the same direction and almost parallel to the surface of a whispering-gallery-mode (WGM) cavity (shown in Supplementary Figure S1). Through the numerical simulation, for example, it is obtained that the azimuthal component of the wave vector is over 13 (14) orders of magnitude higher than the radial component at 1550 nm (775 nm) band in a silica microsphere with a diametre of 60 μm. Note that $\mathbf{E}_{0j}$ follows

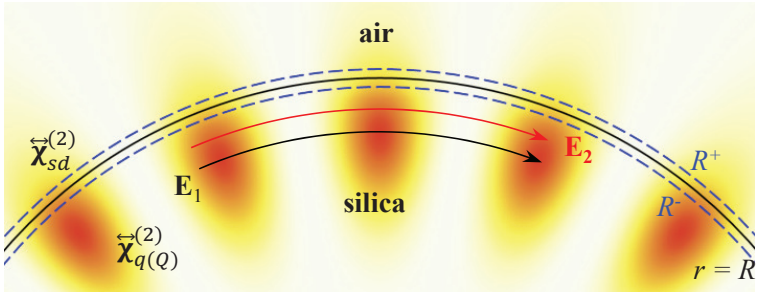

Supplementary Figure S1: **Three-layer model for schematic illustration of SHG.** Electric field of SH $\mathbf{E}_2$ is excited by the pump field $\mathbf{E}_1$ from an interfacial system on a spherical microcavity with a radius of R. The blue dashed curve with the radius of R^- (R^+) stands for the internal (outside) surface of the thin intermediate layer .

the mode field distribution of the WGM cavity, which gives

$$(\nabla^2 - \frac{n_2^2}{c^2}\frac{\partial^2}{\partial t^2})(\mathbf{E}_{02}e^{-i\omega_2 t}) = 0. \tag{S3}$$

Using the slowly varying approximation ($\frac{d^2\tilde{\alpha}_j}{dt^2} \ll \omega_j \frac{d\tilde{\alpha}_j}{dt}$ and $\frac{d\tilde{\alpha}_j}{dt} \ll \omega_j$) in the derivation, equations **S2** - **S3** yield

$$\frac{d\tilde{\alpha}_2}{dt} = ig\tilde{\alpha}_1^2 e^{-i(2\omega_1-\omega_2)t}, \tag{S4}$$

$$g = 2\frac{\omega_1^2}{\omega_2 n_2^2}\frac{\int \mathbf{E}_{02}^* \cdot \mathbf{P}^{(2)} \mathrm{d}V}{\int |\mathbf{E}_{02}|^2 \mathrm{d}V}, \tag{S5}$$

where g is the total nonlinear coupling strength for SHG, and the domain of the volume integral is a spherical space from r=0 to r=R^+. Considering the lossless nonlinear coupling ($d|\tilde{\alpha}_1|^2/dt + d|\tilde{\alpha}_2|^2/dt = 0$), the dynamic evolution of $\tilde{\alpha}_1$ can be written as

$$\frac{d\tilde{\alpha}_1}{dt} = -ig^*\tilde{\alpha}_1^*\tilde{\alpha}_2 e^{-i(\omega_2-2\omega_1)t}. \tag{S6}$$

B. Coupled mode equations and enhancement of SHG

By incorporating the loss and input, the coupled-mode equations are given,

$$\frac{d\tilde{\alpha}_1}{dt} = -\frac{\kappa_{10}+\kappa_{1e}}{2}\tilde{\alpha}_1 + \sqrt{\kappa_{1e}}se^{-i(\omega_p-\omega_1)t} - ig^*\tilde{\alpha}_1^*\tilde{\alpha}_2 e^{-i(\omega_2-2\omega_1)t}, \tag{S7}$$

$$\frac{d\tilde{\alpha}_2}{dt} = -\frac{\kappa_{20}+\kappa_{2e}}{2}\tilde{\alpha}_2 + ig\tilde{\alpha}_1^2 e^{-i(2\omega_1-\omega_2)t}, \tag{S8}$$

where ω_p and s denote the frequency and the amplitude of the input electric field in the pump fibre with $|s|^2$ being the input power; κ_{j0} and κ_{je} represent the intrinsic decay rate and external coupling rate, respectively. In the rotating frame of the pump $\alpha_1 = \tilde{\alpha}_1 e^{i(\omega_p-\omega_1)t}$ and $\alpha_2 = \tilde{\alpha}_2 e^{i(2\omega_p-\omega_2)t}$, the coupled-mode equations can be rewritten as

$$\frac{d\alpha_1}{dt} = [i(\omega_p-\omega_1) - \frac{\kappa_{10}+\kappa_{1e}}{2}]\alpha_1 + \sqrt{\kappa_{1e}}s - ig^*\alpha_1^*\alpha_2, \tag{S9}$$

$$\frac{d\alpha_2}{dt} = [i(2\omega_p-\omega_2) - \frac{\kappa_{20}+\kappa_{2e}}{2}]\alpha_2 + ig\alpha_1^2, \tag{S10}$$

which are the same with equations 2 and 3 in Methods of the main text.

The pump is almost unperturbed by SHG, since the pump light is much stronger than the SH signal. Therefore, the last term in equation **S9** can be ignored in the following analysis. Considering the steady state ($d\tilde{\alpha}_1/dt = d\tilde{\alpha}_2/dt = 0$),

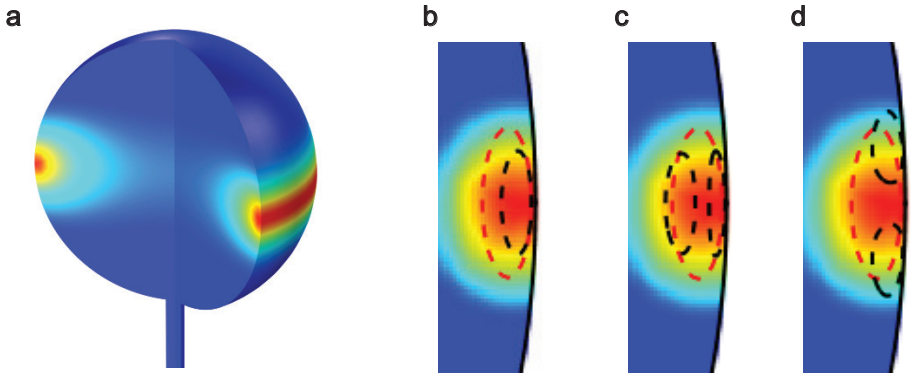

Supplementary Figure S2: **Temperature distribution of a silica microsphere cavity.** **a**, Simulated temperature distribution with the heating source from a fundamental pump mode. **b-d**, Temperature distribution in the meridian plane with a fundamental pump mode profile (red dashed) and a SH mode profile (black dashed). **b**, Fundamental SH mode. **c**, Second-order SH mode in radial direction. **d**, Second-order SH mode in polar direction.

the above coupled mode equations result in the expression of generated SH power,

$$P_2 = \frac{4|g|^2 Q_2^2/Q_{2e}}{\omega_2[4Q_2^2(2\omega_p/\omega_2 - 1)^2 + 1]} \frac{16Q_1^4/Q_{1e}^2}{\omega_1^2[4Q_1^2(\omega_p/\omega_1 - 1)^2 + 1]^2} P_1^2, \tag{S11}$$

where $Q_j = \omega_j/(\kappa_{j0}+\kappa_{je})$ and $Q_{je} = \omega_j/\kappa_{je}$ stand for the loaded quality factor and external (coupling related) quality factor, respectively. The above equation is the same as equation 1 in the main text. In the case of phase-matching (*i.e.*, $\omega_p = \omega_1 = \omega_2/2$) and a given Q_j/Q_{je} (fixed external coupling condition), the conversion efficiency $P_2/P_1^2 \propto Q_2 Q_1^2$. Considering the non-enhancement case with the cavity fineness of 1, the corresponding loaded quality factor is given by $Q_{j,no} = 2\pi n_j R/\lambda_j$, where R is the cavity radius. Consequently, using the experimental parameters from the main text, the conversion efficiency P_2/P_1^2 is enhanced by $\sim 9.5\times10^{13}$ times compared with the non-enhancement case, which is in agreement with the experimental results.

C. Phase matching assisted by thermal and optical Kerr effects

Both thermal expansion and thermal-optical effects contribute to an effective refractive index change coefficient [3] $(\partial n/\partial T)_{\text{eff}}$, and can be written into a thermal-effect-induced nonlinear polarization $\mathbf{P}_{\text{thm}} = \epsilon_0[2n_j(\partial n/\partial T)_{\text{eff}}\Delta T]\mathbf{E}_j$, where ϵ_0 is permittivity of vacuum and n_j is the refractive index for pump (SH) light with $j = 1(2)$. Here $\Delta T(\mathbf{x}, t)$ denotes the variation of temperature distribution. Optical Kerr effect also modulates the refractive index, which can also be treated with a nonlinear polarization $\mathbf{P}_{\text{Kerr}}$. By introducing the nonlinear polarizations into the Helmholtz equation for the pump and the SH modes, we can obtain the shifted resonance frequencies $\omega_1 = \omega_{10} - B_{11}|\alpha_1|^2$ and $\omega_2 = \omega_{20} - B_{12}|\alpha_1|^2$, with

$$B_{11} = [\frac{3\chi_{\text{Kerr}}\omega_1}{n_1^2} + (\frac{\partial n}{\partial T})_{\text{eff}} \frac{\epsilon_0}{\rho C \delta_T} \frac{\omega_1^2 n_1}{Q_{1,\text{abs}}}] \frac{\int |\mathbf{E}_{01}|^4 d\mathbf{V}}{\int |\mathbf{E}_{01}|^2 d\mathbf{V}}, \tag{S12}$$

$$B_{12} = [\frac{6\chi_{\text{Kerr}}\omega_2}{n_2^2} + (\frac{\partial n}{\partial T})_{\text{eff}} \frac{\epsilon_0}{\rho C \delta_T} \frac{\omega_1\omega_2 n_1^2}{n_2 Q_{1,\text{abs}}}] \frac{\int |\mathbf{E}_{01}|^2 |\mathbf{E}_{02}|^2 d\mathbf{V}}{\int |\mathbf{E}_{02}|^2 d\mathbf{V}}, \tag{S13}$$

where χ_{Kerr} is the Kerr nonlinear susceptibility, and ρ denotes the density of cavity; C is the specific heat capacity, δ_T represents the thermal relaxing rate [4], and $Q_{1,\text{abs}}$ is the cavity quality factor related to absorption loss which is the source of the light-induced heating. The thermal and Kerr effects of the SH are ignored since the power of SH is much weaker than that of the pump.

Using equations **S12** and **S13**, the rates of frequency shifts can be compared for the SH mode and the pump mode. Generally, thermal effect accounts for a dominant part of the frequency shift for both modes. If the temperature distribution is homogeneous throughout the cavity, B_{12} and $2B_{11}$ will be very close, and the perfect phase-matching will be difficult. Fortunately, by taking into account the temperature distribution along the radial and polar direction in the cavity (Supplementary Figure **S2**), the temperature distribution overlaps perfectly with the pump cavity mode but does not with the SH mode, and consequently $B_{12} < 2B_{11}$. Note that here the temperature-dependent Sellmeier

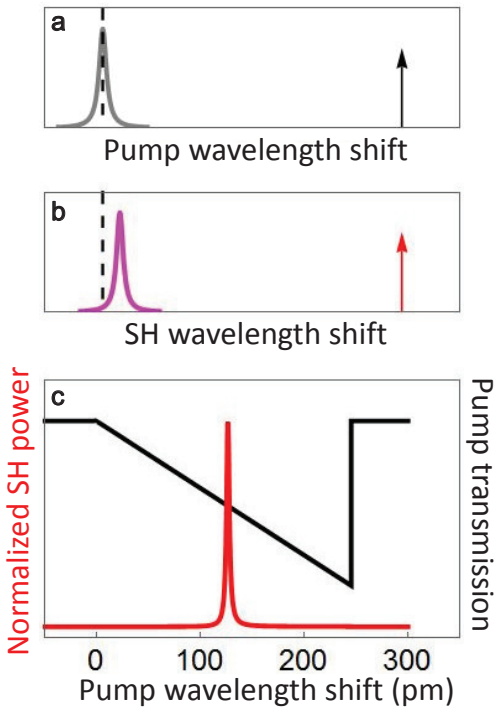

Supplementary Movie S1 (online): **Dynamic phase-matching process. a** (**b**), Pump (SH) light wavelength shift relative to the wavelength of the pump (SH) cold cavity mode. The black (red) arrow represent the pump light (its SH) wavelength. The grey (magenta) Lorentzian shape stands for the pump (SH) cavity mode. **c**, Pump transmission (black curve) and normalized SH power (red curve) versus the pump wavelength shift.

coefficients and chromatic dispersions are already involved [5]. As an example, the coefficients are calculated within a microsphere (diametre $\sim$ 62 μm) by using a pair of modes that are nearly phase-matched. The pump mode is a fundamental mode with radial (q_1), angular (l_1) and azimuthal (m_1) numbers of 1, 171 and 171. For the SH mode, $q_2 = 2$ (to achieve preliminary phase-matching [6]) and $l_2 = m_2 = 342$. In this case, the ratio of frequency shifts induced by thermal and Kerr effects are 52 and 119 for the pump mode and the SH mode, respectively. Besides, $2B_{11}/B_{12} = 1.028$, manifesting that the rate of the frequency shift for the SH mode is slower than twice the rate of the shift for the pump mode. Furthermore, it is evident to obtain the relation $\Delta\omega_2 < 2\Delta\omega_1 < 2\Delta\omega_p$, which is the condition for the SH signal to catch the SH mode in the phase-matching process. The phase-matching process within a full tuning range is dynamically shown in Supplementary Movie **S1 (online)**.

It should be noted that in the process of mode shift induced by the thermal and Kerr effects, the pump light always tracks on the same resonance, as well as the SH signal. First, in a cavity with the thermal and Kerr effects, all of the modes will experience red shifts as the intracavity power increases. Second, for the SH mode, a single peak of SH power (shown in Figures 2b and c of the main text, as well as Supplementary Movie **S1 (online)**) confirms that the SH signal passes through only one cavity mode. If the mode-jump occurred, two or more perfect phase-matching points could be achieved, and more peaks could be observed in Figures 2b and c. For the pump mode, the mode-jump phenomenon may occur in transmission measurements of microcavities . However, in the experiment presented in this work, the mode-jump is not observed in the transmission spectrum, because the transmission changes continuously with the increasing or decreasing pump wavelength, instead of a discrete change in the transmission. Even if in other cases when the mode-jump takes place for the pump mode, the succeeding mode also can be used for the perfect phase-matching (double resonances).

II. DEPENDENCE OF SECOND-HARMONIC POWER ON THE PUMP POWER

As described in the main text, the phase-matching method introduces a critical power in SHG. The process to obtain the power-dependent curve is illustrated in Supplementary Figure **S3**b. With different pump wavelengths, the maximum SH power is recorded (shown by the blue dots in Supplementary Figure **S3**a). Note that both in the measurement and the theoretical calculation, the SH power at any detuning is recorded in a steady state. Above the

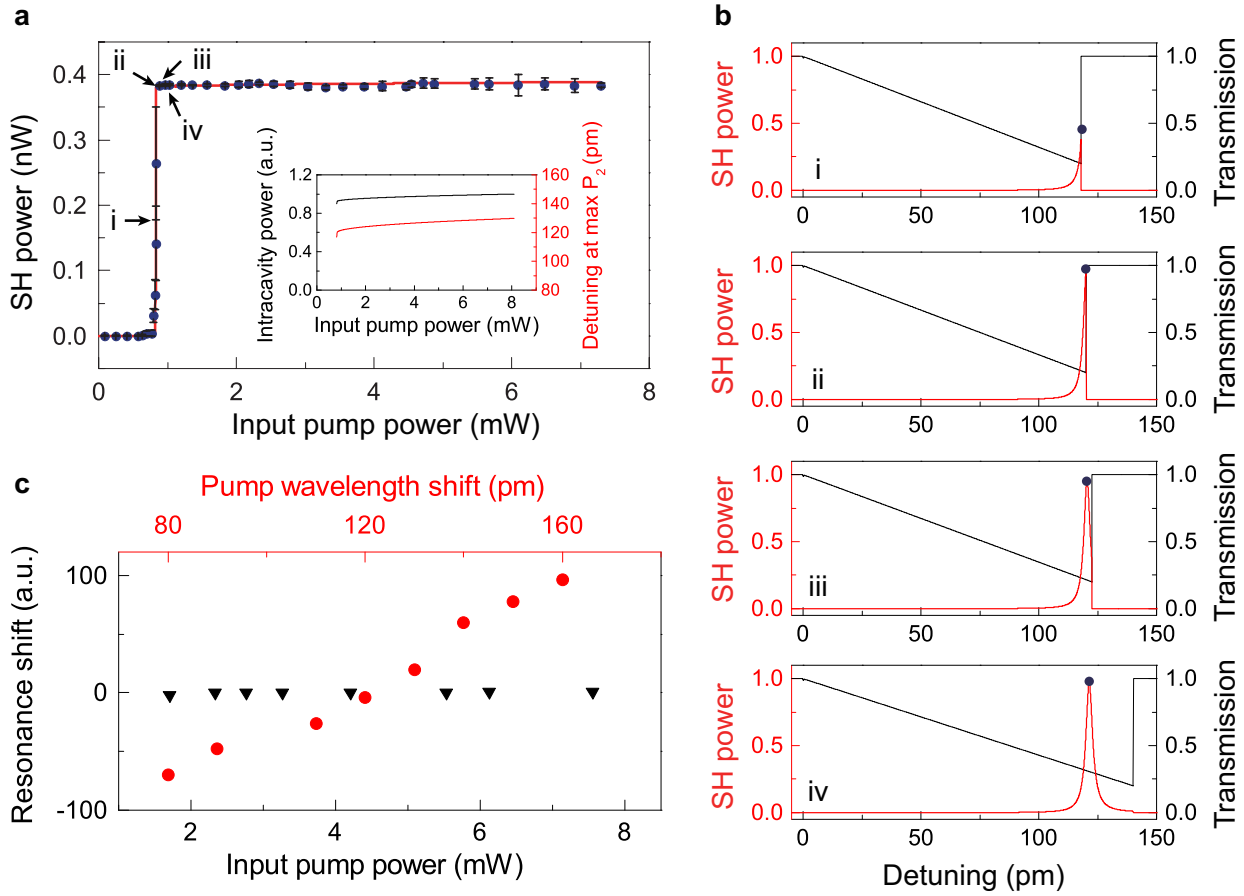

Supplementary Figure S3: **Dependence of SH power on the pump power. a,** Measured and theoretical SH power versus the input pump power (the same as Figure 2**d** in the main text). Inset: Theoretically calculated intracavity power (black) and the pump-cold-cavity-mode detuning (red) with maximum SH power versus the input power. **b,** Theoretically calculated SH power (red solid curve) and the pump transmission (black dashed curve) versus the detuning at four fixed input power corresponding to i-iv in **a. c,** Measured resonance shift of an SH mode near 780 nm with changing input power at the pump-cold-cavity-mode detuning of 120 pm (black triangle) and with changing pump wavelength at the pump power of 1.7 mW (red circle).

critical power, the increasing input power at a given frequency pushes the pump mode farther to the red side (the pump is not completely on resonance) and consequently increases the detuning between the pump light and the cavity mode.

The reduced enhancement of the pump light counteracts with the increasing input power, leading to the almost steady intracavity energy. The on-resonance wavelength of the SH mode also remains stable so that the intracavity energy and consequently the SH power at this wavelength are almost stable as well (shown in the inset of Supplementary Figure **S3**a). To confirm that the increasing of intracavity power is negligible with the increasing input power at a certain wavelength, we measure the resonance shift of a cavity mode near 780 nm with (i) increasing input power at a fixed wavelength, (ii) increasing pump wavelength at a fixed pump power. The resonance shift in the first case is almost unresolvable, which represents the almost stable intracavity power in this case, as shown in Supplementary Figure **S3**c. It is also possible to obtain the explicit $P_2 \propto P_1^2$ dependence by introducing a new degree of freedom, such as an external heater, to manipulate the SH mode frequency and consequently reach double resonances with various intracavity energies.

III. IDENTIFICATION OF SYMMETRY-BREAKING-INDUCED NONLINEARITY AND PURE BULK RESPONSES

The emergence of the surface can generate SH due to both the surface ED contribution and the EQ contributions related to the surface-induced symmetry breaking. The latter includes the contributions from the rapid variation of the electric field at the surface and the longitudinal electric-polarization at the surface, which are demonstrated in Section **III-B**. The above symmetry-breaking-induced nonlinearity depends on the existence of a surface and is irrelevant to the electric field in the bulk, which can be used to study the surface properties. In contrast, the pure bulk EQ response is merely caused by the gradient of the mode field in the bulk.

The symmetry-breaking-induced nonlinearity on the surface can be distinguished from the pure bulk nonlinear response under the transverse-electric (TE) polarized pump. The method of the identification can be understood with some physical reasoning by analysing the polarization response. In a microsphere cavity with a diametre greater than dozens of microns, the electric field of a TE mode is mainly along the polar direction ($E_\theta\hat{\mathbf{e}}_\theta$, parallel to the surface), while a transverse magnetic (TM) mode has two main electric-field components along the radial ($E_r\hat{\mathbf{e}}_r$, perpendicular to the surface) and azimuthal ($E_\phi\hat{\mathbf{e}}_\phi$, parallel to the surface) direction, respectively. Since the major electric-field component is about two orders of magnitude larger than the minor component, the azimuthal (polar) electric field of a TE (TM) mode can be neglected for approximation. In this case, the symmetry-breaking-induced nonlinearity requires at least one TM polarized wave with the radial component of the electric field to break the symmetry at the surface. Therefore, the only possible SH from symmetry-breaking-induced nonlinearity is TM polarized under the TE pump. As for the bulk contribution, the TM polarized SH is forbidden. This is because the wave vectors of both pump and SH modes are collinear, and the bulk contribution will vanish once the polarizations of pump and SH light are orthogonal. In this view, the only possible SH is TE polarized from the pure bulk contribution. Considering the non-degenerate TE and TM modes in frequency domain for a microsphere cavity, the excited SH can be either from the surface-induced symmetry-breaking or the pure bulk response, but never both of them. Thus, the symmetry-breaking-induced nonlinearity and the pure bulk quadrupole contribution can be distinguished successfully. Here we would emphasize that what we identified is the symmetry-breaking-induced nonlinearity at the surface, instead of the conventional surface nonlinearity, as explained below.

The specific proof in detail is derived as follows. In Section **III-A**, we show the expressions of different nonlinear coupling strengths. In Sections **III-B** and **C**, we discuss the properties of the SH signals from different origins under TE and TM pumps. Section **III-D** shows the comparison of the conventional surface nonlinear optics and the surface symmetry-breaking-induced nonlinearity in WGM microcavities. Section **III-E** presents the experimental details for the identification.

A. Nonlinear coupling strength

The different origins of SH signals can be described by the nonlinear coupling strength g. Considering the nonlinear electric polarization in equation **S1**, the susceptibilities tensor $\overleftrightarrow{\boldsymbol{\chi}}^{(2)}_{\mathrm{sd}}$ consists of three non-zero components $\chi^{(2)}_{\mathrm{sd},\perp\perp\perp}$, $\chi^{(2)}_{\mathrm{sd},\perp\parallel\parallel}$ and $\chi^{(2)}_{\mathrm{sd},\parallel\parallel\perp}$ [7]. Here, the first polarization subscript of the tensor component stands for the SH, and the other two are for the pump, which follow the convention description. As for the susceptibilities tensor $\overleftrightarrow{\boldsymbol{\chi}}^{(2)}_{\mathrm{q}}$ and $\overleftrightarrow{\boldsymbol{\chi}}^{(2)}_{\mathrm{Q}}$ in the bulk with isotropic material, the corresponding non-zero elements are ($\chi^{(2)}_{\mathrm{q},i(\bar{j}\bar{j})i}$, $\chi^{(2)}_{\mathrm{q},i(\bar{j}i)j}$, $\chi^{(2)}_{\mathrm{q},i(\bar{i}\bar{j})j}$) and ($\chi^{(2)}_{\mathrm{Q},(\bar{i}\bar{j})ij}$, $\chi^{(2)}_{\mathrm{Q},(\bar{i}\bar{j})ji}$, $\chi^{(2)}_{\mathrm{Q},(\bar{i}i)jj}$) [1, 7], where the repeated subscripts mean that the corresponding two unit vectors do inner product and the bars denote the one from gradient operator. The subscripts $i \neq j$ refer to the orthogonal coordinates, and the bracketed subscripts denote the coordinates associated with the EQ tensor elements. Here is an example to illustrate the operational rule, $\hat{\mathbf{e}}_1 \cdot \overleftrightarrow{\boldsymbol{\chi}}^{(2)}_{\mathrm{q}} : \nabla\hat{\mathbf{e}}_2\hat{\mathbf{e}}_3 = (\hat{\mathbf{e}}_1\cdot\hat{\mathbf{e}}_3)(\nabla\cdot\hat{\mathbf{e}}_2)\chi^{(2)}_{\mathrm{q},i(\bar{j}\bar{j})i} + [(\hat{\mathbf{e}}_3\cdot\nabla)\hat{\mathbf{e}}_2)]\cdot\hat{\mathbf{e}}_1\chi^{(2)}_{\mathrm{q},i(\bar{j}i)j} + [(\hat{\mathbf{e}}_1\cdot\nabla)\hat{\mathbf{e}}_2)]\cdot\hat{\mathbf{e}}_3\chi^{(2)}_{\mathrm{q},i(\bar{i}\bar{j})j}$. For the first term, the first and the fourth positions of the subscripts denote $\hat{\mathbf{e}}_1$ and $\hat{\mathbf{e}}_3$, and the same i means the inner product between $\hat{\mathbf{e}}_1$ and $\hat{\mathbf{e}}_3$. On the other hand, $\bar{j}$ at the second position denotes ∇ and the third position denotes $\hat{\mathbf{e}}_2$, and the same j means do an inner product $\nabla\cdot\hat{\mathbf{e}}_2$. For all three terms, the parentheses is always on the second and third positions, meaning that ∇ always acts on $\hat{\mathbf{e}}_2$. In this case, it is feasible to distinguish the origins of SH signal by analysing the pump polarization and the SH mode field distribution along the polar direction.

By inserting equation S1 into equation S5, the specific form of total coupling strength g is given as

$$\begin{aligned}\int \mathbf{E}_{02}^{*}\cdot\mathbf{P}^{(2)}\mathrm{d}V &= \int_0^{2\pi}\int_0^{\pi}\int_0^{R^+}\mathbf{E}_{02}^{*}\cdot[\overleftrightarrow{\chi}_{\mathrm{d}}^{(2)}:\mathbf{E}_{01}\mathbf{E}_{01}+2\overleftrightarrow{\chi}_{\mathrm{q}}^{(2)}:\nabla\mathbf{E}_{01}\mathbf{E}_{01}-\nabla\cdot(\overleftrightarrow{\chi}_{\mathrm{Q}}^{(2)}:\mathbf{E}_{01}\mathbf{E}_{01})]\mathrm{d}V\\ &= \int_0^{2\pi}\int_0^{\pi}\int_0^{R^+}[\mathbf{E}_{02}^{*}\cdot\overleftrightarrow{\chi}_{\mathrm{d}}^{(2)}:\mathbf{E}_{01}\mathbf{E}_{01}+2\mathbf{E}_{02}^{*}\cdot\overleftrightarrow{\chi}_{\mathrm{q}}^{(2)}:\nabla\mathbf{E}_{01}\mathbf{E}_{01}+\nabla\mathbf{E}_{02}^{*}:\overleftrightarrow{\chi}_{\mathrm{Q}}^{(2)}:\mathbf{E}_{01}\mathbf{E}_{01}\\ &\quad-\nabla\cdot(\mathbf{E}_{02}^{*}\cdot\overleftrightarrow{\chi}_{\mathrm{Q}}^{(2)}:\mathbf{E}_{01}\mathbf{E}_{01})]\mathrm{d}V.\end{aligned}\tag{S14}$$

Note that here the normalized denominator and other constants in equation S5 are neglected for convenience. The first term on the right-hand side of equation S14 is simplified as a surface integral on a microsphere,

$$\begin{aligned}\int_0^{2\pi}\int_0^{\pi}\int_0^{R^+}\mathbf{E}_{02}^{*}\cdot\overleftrightarrow{\chi}_{\mathrm{d}}^{(2)}:\mathbf{E}_{01}\mathbf{E}_{01}\mathrm{d}V &= \int_0^{2\pi}\int_0^{\pi}\int_0^{R^+}\mathbf{E}_{02}^{*}\cdot\overleftrightarrow{\chi}_{\mathrm{sd}}^{(2)}\delta(r-R):\mathbf{E}_{01}\mathbf{E}_{01}\mathrm{d}V\\ &= \int_{\mathrm{surface},r=R}\mathbf{E}_{02}^{*}\cdot\overleftrightarrow{\chi}_{\mathrm{sd}}^{(2)}:\mathbf{E}_{01}\mathbf{E}_{01}\mathrm{d}S\equiv g_{\mathrm{sd}},\end{aligned}\tag{S15}$$

where g_{sd} is the coupling strength for surface-dipolar nonlinearity.

As for the second and third terms on the right-hand side of equation S14, the EQ responses are induced by the spatial variation of the electric field. The corresponding integral can be divided into the surface domain ($r\in[R^-,R^+]$) and bulk domain ($r\in[0,R^-)$), *i.e.*,

$$\int_0^{2\pi}\int_0^{\pi}\left(\int_{R^-}^{R^+}+\int_0^{R^-}\right)(2\mathbf{E}_{02}^{*}\cdot\overleftrightarrow{\chi}_{\mathrm{q}}^{(2)}:\nabla\mathbf{E}_{01}\mathbf{E}_{01}+\nabla\mathbf{E}_{02}^{*}:\overleftrightarrow{\chi}_{\mathrm{Q}}^{(2)}:\mathbf{E}_{01}\mathbf{E}_{01})\mathrm{d}V.\tag{S16}$$

The last integral term on the right-hand side in equation S14 can be rewritten by utilizing Gauss formula as a surface integral,

$$\int_0^{2\pi}\int_0^{\pi}\int_0^{R^+}\nabla\cdot(\mathbf{E}_{02}^{*}\cdot\overleftrightarrow{\chi}_{\mathrm{Q}}^{(2)}:\mathbf{E}_{01}\mathbf{E}_{01})\mathrm{d}V=\int_{\mathrm{surface},r=R^+}(\mathbf{E}_{02}^{*}\cdot\overleftrightarrow{\chi}_{\mathrm{Q}}^{(2)}:\mathbf{E}_{01}\mathbf{E}_{01})\cdot\mathrm{d}\mathbf{S}=0.\tag{S17}$$

Since the integral domain is the outside surface of the microsphere and $\overleftrightarrow{\chi}_{\mathrm{Q}}^{(2)}(R^+)$ follows the nonlinearity of air, this integral value in equation S17 vanishes. As a result, the total nonlinear coupling strength (in equation S5) can be expressed as the sum of equations S15 and S16.

B. Pump mode with TE polarization

With the TE polarized pump, we consider the main component of the electric field, $\mathbf{E}_{01}=E_{01,\theta}(r,\theta,\phi)\hat{\mathbf{e}}_\theta$ (r,θ,ϕ are the standard spherical coordinates), which is parallel to the surface. Although the azimuthal electric field also exists, such a component can be neglected due to the extremely weak amplitude (nearly two orders of magnitude weaker). As aforementioned, the SH signals involve different kinds of contributions, each of which corresponds to a nonlinear coupling strength. First, for the surface dipole response g_{sd} (equation S15), the susceptibility component $\chi_{\mathrm{sd},\perp\parallel\parallel}^{(2)}$ mediates the nonlinear coupling, giving rise to TM polarized SH. Due to the symmetry of the cavity geometry along the polar direction, g_{sd} is non-zero only if SH electric field $E_{02}(r,\theta,\phi)$ exhibits an even polar distribution with the product of $E_{01,\theta}E_{01,\theta}$ which is also an even function of θ. Here the odevity is in terms of the axis of $\theta=\pi/2$, similarly hereinafter. Note that an even (odd) polar distribution of the electric field means that the number of local maximum of the intensity along the polar direction is odd (even).

Second, for the surface-related part in equation S16, the specific form of both the pump and SH modes electric field should be analysed. The TE pump mode only has the polar component, given as

$$\mathbf{E_{01}}=E_{01,\theta}\hat{\mathbf{e}}_\theta=-\frac{m_1}{\sin\theta}\psi_{l_1}(n\frac{\omega_1}{c}r)Y_{l_1}^{m_1}(\theta,\phi)\hat{\mathbf{e}}_\theta,\tag{S18}$$

where $\psi_l(r)$ is normalized spherical Bessel (Hankel) function of the first kind for inside-cavity (outside-cavity) field with n being the refraction index of silica (air) , Y_l^m is spherical harmonic function and $\hat{\mathbf{e}}_\theta$ is the polar unit vector. It is evident that the electric field of a TE mode is continuous across the surface, while it is not true for a TM mode.

Back to the surface domain part in equation S16, the expression with a TE pump mode is given as,

$$\int_0^{2\pi}\int_0^{\pi}\int_{R^-}^{R^+}[2\mathbf{E}_{02}^*\cdot\overleftrightarrow{\chi}_{\mathrm{q}}^{(2)}:(\nabla E_{01,\theta}\hat{\mathbf{e}}_\theta)E_{01,\theta}\hat{\mathbf{e}}_\theta+\nabla\mathbf{E}_{02}^*:\overleftrightarrow{\chi}_{\mathrm{Q}}^{(2)}:E_{01,\theta}\hat{\mathbf{e}}_\theta E_{01,\theta}\hat{\mathbf{e}}_\theta]\mathrm{d}V. \tag{S19}$$

Since the volume of the integral domain is zero, the integral of a bounded function also consequently vanishes. In the case of the continuous field $E_{01,\theta}$, the value of equation S19 remains zero unless $\mathbf{E}_{02}$ is discontinuous at the surface. Therefore, equation S19 can be simplified as,

$$\int_0^{2\pi}\int_0^{\pi}\int_{R^-}^{R^+}(\frac{\partial}{\partial r}\hat{\mathbf{e}}_{\mathbf{r}}E_{02,r}^*\hat{\mathbf{e}}_{\mathbf{r}}:\overleftrightarrow{\chi}_{\mathrm{Q}}^{(2)}:E_{01,\theta}\hat{\mathbf{e}}_\theta E_{01,\theta}\hat{\mathbf{e}}_\theta)\mathrm{d}V. \tag{S20}$$

The discontinuous $E_{02,r}$ is provided by a TM polarized SH mode, and has a distribution form,

$$\begin{aligned}E_{02,r}=\frac{D_{02,r}}{\varepsilon_r}&=\frac{1}{\varepsilon_r\sqrt{\varepsilon_0}}\frac{l_2(l_2+1)c}{\omega_2 r}\psi_{l_2}(n\frac{\omega_2}{c}r)Y_{l_2}^{m_2}(\theta,\phi)\\&=[(1-\frac{1}{n_s^2})h(r-R)+\frac{1}{n_s^2}]\frac{1}{\sqrt{\varepsilon_0}}\frac{l_2(l_2+1)c}{\omega_2 r}\psi_{l_2}(n\frac{\omega_2}{c}r)Y_{l_2}^{m_2}(\theta,\phi),\end{aligned} \tag{S21}$$

where $D_{02,r}$ is the electric displacement field, ε_r (n_s) is relative dielectric constant (refraction index) of silica, and $h(r)$ is Heaviside step function. Based on the form of $E_{02,r}$ in equation S21, we can rewrite equation S20 as,

$$\begin{aligned}&\int_0^{2\pi}\int_0^{\pi}\int_{R^-}^{R^+}[(1-\frac{1}{n_s^2})\delta(r-R)\hat{\mathbf{e}}_{\mathbf{r}}D_{02,r}^*\hat{\mathbf{e}}_{\mathbf{r}}:\overleftrightarrow{\chi}_{\mathrm{Q}}^{(2)}:E_{01,\theta}\hat{\mathbf{e}}_\theta E_{01,\theta}\hat{\mathbf{e}}_\theta]\mathrm{d}V\\&=\int_{\mathrm{surface},r=R}[(1-\frac{1}{n_s^2})\hat{\mathbf{e}}_{\mathbf{r}}D_{02,r}^*\hat{\mathbf{e}}_{\mathbf{r}}:\overleftrightarrow{\chi}_{\mathrm{Q}}^{(2)}:E_{01,\theta}\hat{\mathbf{e}}_\theta E_{01,\theta}\hat{\mathbf{e}}_\theta]\mathrm{d}S\\&=\int_{\mathrm{surface},r=R}[(1-\frac{1}{n_s^2})D_{02,r}^*E_{01,\theta}E_{01,\theta}(\hat{\mathbf{e}}_{\mathbf{r}}\cdot\hat{\mathbf{e}}_{\mathbf{r}})(\hat{\mathbf{e}}_\theta\cdot\hat{\mathbf{e}}_\theta)\chi_{\mathrm{Q},(\bar{i}i)jj}^{(2)}]\mathrm{d}S\\&=\int_{\mathrm{surface},r=R}[(1-\frac{1}{n_s^2})D_{02,r}^*E_{01,\theta}E_{01,\theta}\chi_{\mathrm{Q},(\bar{i}i)jj}^{(2)}]\mathrm{d}S\equiv g_{\mathrm{s,var}}.\end{aligned} \tag{S22}$$

It is found that the coupling $g_{\mathrm{s,var}}$ is from the rapid variation of electric filed at the surface, and induces a SH signal with a TM polarization and an even polar distribution of the mode field, the reason of which is similar to that induced by g_{sd}. Note that this contribution originates from the variation of the EQ susceptibility across the surface, which is absent within the bulk due to the homogeneity of the material.

Apart from the surface domain part in equation S16, the rest with a continuous integrand can be written as,

$$\begin{aligned}&\int_0^{2\pi}\int_0^{\pi}\int_0^{R^-}[2\mathbf{E}_{02}^*\cdot\overleftrightarrow{\chi}_{\mathrm{q}}^{(2)}:(\nabla\mathbf{E}_{01})\mathbf{E}_{01}+\nabla\mathbf{E}_{02}^*:\overleftrightarrow{\chi}_{\mathrm{Q}}^{(2)}:\mathbf{E}_{01}\mathbf{E}_{01}]\mathrm{d}V\\&=\int_0^{2\pi}\int_0^{\pi}\int_0^{R^-}\{2[(\mathbf{E}_{02}^*\cdot\nabla)\mathbf{E}_{01}]\cdot\mathbf{E}_{01}\chi_{\mathrm{q},i(\bar{i}j)j}^{(2)}+2(\mathbf{E}_{02}^*\cdot\mathbf{E}_{01})(\nabla\cdot\mathbf{E}_{01})\chi_{\mathrm{q},i(\bar{j}j)i}^{(2)}\\&+2[(\mathbf{E}_{01}\cdot\nabla)\mathbf{E}_{01}]\cdot\mathbf{E}_{02}^*\chi_{\mathrm{q},i(\bar{j}i)j}^{(2)}\}\mathrm{d}V+\\&\int_0^{2\pi}\int_0^{\pi}\int_0^{R^-}\{(\nabla\cdot\mathbf{E}_{02}^*)(\mathbf{E}_{01}\cdot\mathbf{E}_{01})\chi_{\mathrm{Q},(\bar{i}i)jj}^{(2)}+[(\mathbf{E}_{01}\cdot\nabla)\mathbf{E}_{02}^*]\cdot\mathbf{E}_{01}\chi_{\mathrm{Q},(\bar{i}j)ij}^{(2)}\\&+[(\mathbf{E}_{01}\cdot\nabla)\mathbf{E}_{02}^*]\cdot\mathbf{E}_{01}\chi_{\mathrm{Q},(\bar{i}j)ji}^{(2)}\}\mathrm{d}V.\end{aligned} \tag{S23}$$

Since the free electric charge is absent, $\nabla\cdot\mathbf{E}$ terms vanish. The first integral in equation S23 can be further simplified as,

$$\int_0^{2\pi}\int_0^{\pi}\int_0^{R^-}\{\mathbf{E}_{02}^*\cdot\nabla(\mathbf{E}_{01}\cdot\mathbf{E}_{01})\chi_{\mathrm{q},i(\bar{i}j)j}^{(2)}+2[(\mathbf{E}_{01}\cdot\nabla)\mathbf{E}_{01}]\cdot\mathbf{E}_{02}^*\chi_{\mathrm{q},i(\bar{j}i)j}^{(2)}\}\mathrm{d}V. \tag{S24}$$

The first term in equation **S24** involves a longitudinal wave field, and can be transformed to a surface integral, *i.e.*,

$$\begin{aligned}\int_0^{2\pi}\int_0^{\pi}\int_0^{R^-}\mathbf{E}_{02}^*\cdot\nabla(\mathbf{E}_{01}\cdot\mathbf{E}_{01})\chi^{(2)}_{\mathrm{q},i(\bar{i}j)j}\mathrm{d}V &= \int_0^{2\pi}\int_0^{\pi}\int_0^{R^-}\{\nabla\cdot[\mathbf{E}_{02}^*(\mathbf{E}_{01}\cdot\mathbf{E}_{01})]-(\nabla\cdot\mathbf{E}_{02}^*)(\mathbf{E}_{01}\cdot\mathbf{E}_{01})\}\chi^{(2)}_{\mathrm{q},i(\bar{i}j)j}\mathrm{d}V\\ &= \int_0^{2\pi}\int_0^{\pi}\int_0^{R^-}\nabla\cdot[\mathbf{E}_{02}^*(\mathbf{E}_{01}\cdot\mathbf{E}_{01})]\chi^{(2)}_{\mathrm{q},i(\bar{i}j)j}\mathrm{d}V\\ &= \int_{\mathrm{surface},r=R^-}\mathbf{E}_{02}^*(\mathbf{E}_{01}\cdot\mathbf{E}_{01})\chi^{(2)}_{\mathrm{q},i(\bar{i}j)j}\cdot\mathrm{d}\mathbf{S}\\ &= \int_{\mathrm{surface},r=R^-}E_{02,r}^*(E_{01,\theta}E_{01,\theta})\chi^{(2)}_{\mathrm{q},i(\bar{i}j)j}\mathrm{d}S\equiv g_{\mathrm{s,long}}.\end{aligned} \tag{S25}$$

Interestingly, although the longitudinal source electric-polarization term $\nabla(\mathbf{E}_{01}\cdot\mathbf{E}_{01})$ comes from the spatial gradient of a mode field, the SH signal from $g_{\mathrm{s,long}}$ is only determined by the mode field at the surface and is irrelevant to the gradient of the mode field in the bulk. Different from the plane wave case where the non-zero component of longitudinal polarization is only in the propagation direction, the longitudinal source electric-polarization $\nabla(\mathbf{E}_{01}\cdot\mathbf{E}_{01})$ contains three components benefiting from the mode distribution $E_{01}(r,\theta,\phi)$. Therefore, the radiation of SH can be generated at the surface due to the radial component of the longitudinal polarization, and this SH mode should be TM polarized to provide a radial electric field. Furthermore, the corresponding SH signal has an even polar distribution, which can be deduced from equation **S25**.

The second term in equation **S24** is shown as follows,

$$\int_0^{2\pi}\int_0^{\pi}\int_0^{R^-}2[(\mathbf{E}_{01}\cdot\nabla)\mathbf{E}_{01}]\cdot\mathbf{E}_{02}^*\chi^{(2)}_{\mathrm{q},i(\bar{j}i)j}\mathrm{d}V=\int_0^{2\pi}\int_0^{\pi}\int_0^{R^-}2E_{02,\theta}^*E_{01,\theta}\frac{\partial}{r\partial\theta}E_{01,\theta}\chi^{(2)}_{\mathrm{q},i(\bar{j}i)j}\mathrm{d}V\equiv g_{\mathrm{b1}}. \tag{S26}$$

The nonlinear coupling g_{b1} works as a pure bulk response, caused by the spatial variation of the mode field in polar direction. Different from the SH signals aforementioned, the coupling channel from g_{b1} is available only if the electric field of SH mode holds an odd polar distribution and TE polarization. It can be understood from the fact that the gradient operation along the polar direction can change the odevity of a function of θ.

Finally, we investigate the second integral in equation **S23** and obtain that,

$$\begin{aligned}&\int_0^{2\pi}\int_0^{\pi}\int_0^{R^-}\{[(\mathbf{E}_{01}\cdot\nabla)\mathbf{E}_{02}^*]\cdot\mathbf{E}_{01}\chi^{(2)}_{\mathrm{Q},(\bar{i}j)ij}+[(\mathbf{E}_{01}\cdot\nabla)\mathbf{E}_{02}^*]\cdot\mathbf{E}_{01}\chi^{(2)}_{\mathrm{Q},(\bar{i}j)ji}\}\mathrm{d}V\\ &=\int_0^{2\pi}\int_0^{\pi}\int_0^{R^-}E_{01,\theta}E_{01,\theta}\frac{\partial}{r\partial\theta}E_{02,\theta}^*(\chi^{(2)}_{\mathrm{Q},(\bar{i}j)ij}+\chi^{(2)}_{\mathrm{Q},(\bar{i}j)ji})\mathrm{d}V\equiv g_{\mathrm{b2}}.\end{aligned} \tag{S27}$$

Similar to g_{b1}, the coupling g_{b2} from $\hat{\theta}$-variation in bulk can also induce a SH mode with a TE polarization and an odd polar distribution. Thus, we use $g_{\mathrm{B}}=g_{\mathrm{b1}}+g_{\mathrm{b2}}$ to denote the nonlinear coupling from the pure bulk EQ responses. Note that it is different from the conventional case on surface SHG that here a TM polarized SH mode with the radial component is forbidden in g_{B}, because the wave vectors of $\mathbf{E}_{01}$ and $\mathbf{E}_{02}$ are collinear for the WGMs under the perfect phase-matching condition, as aforementioned. In this condition, the non-zero bulk nonlinear susceptibility requires the SH electric field to be in the same direction with the pump.

Consequently, the total nonlinear coupling strength contains four components, *i.e.*, $g=g_{\mathrm{sd}}+g_{\mathrm{s,var}}+g_{\mathrm{s,long}}+g_{\mathrm{B}}$, which come from four different physical origins: (*i*) an electric-dipole contribution from the surface layer g_{sd}; (*ii*) an electric-quadrupole contribution from the rapid field variation of the electric field along radial direction at the surface $g_{\mathrm{s,var}}$; (*iii*) an electric-quadrupole contribution from a longitudinal source electric-polarization at the surface $g_{\mathrm{s.long}}$; (*iv*) an electric-quadrupole contribution due to the electric field gradient along polar direction in the bulk g_{B}. Among these origins, the coupling channels g_{sd}, $g_{\mathrm{s,var}}$ and $g_{\mathrm{s,long}}$ rely on the emergence of a surface and can be directly influenced by the surface properties. In this view, the surface-dipole response g_{sd}, together with $g_{\mathrm{s,var}}$ and $g_{\mathrm{s,long}}$, can be attributed to a collective coupling strength $g_{\mathrm{SB}}=g_{\mathrm{sd}}+g_{\mathrm{s,var}}+g_{\mathrm{s,long}}$, which is related to the surface and the consequent symmetry-breaking. In contrast, the nonlinear coupling strength g_{B} only depends on the gradient of the mode field in the bulk, which is a pure bulk response in SHG. Under the TE polarized pump, it is found from the aforementioned discussion that the SH signals from g_{SB} possess even polar distributions and TM polarizations of the field, while the signals from g_{B} hold the odd polar distribution with TE polarizations. Therefore, the symmetry-breaking induced response g_{SB} can be distinguished from bulk response g_{B} by analysing the number of local maxima of SH mode intensity in the polar direction or the polarization of SH under TE pump.

The validity of the approximation that minor components of the field are neglected can be estimated. Through a semiquantitative estimation for the case where the symmetry-breaking-induced SH is expected, it is found that the resulting deviation from bulk is about 10^{-3} weaker than the symmetry-breaking-induced contribution on SH intensity under the experimental condition. On the other hand, when the SH of pure bulk EQ nonlinearity is expected, the symmetry-breaking-induced nonlinear signals cannot disturb the signal of the pure bulk response with TE polarization.

C. Pump mode with TM polarization

When the pump mode is TM polarized, the electric field is mainly along both the radial and azimuthal direction. The properties of the corresponding SH modes could be obtained through the similar approaches aforementioned. However, the more electric field components and more involving susceptibilities give rise to complex and miscellaneous results. In this case, it is indistinguishable for symmetry-breaking-induced nonlinearity and pure bulk EQ response by analysing the polarization and field distribution. The polar field distributions of the SH modes with different polarizations of pump modes are summarized in Supplementary Table **S1**.

Supplementary Table S1: Odevity (even or odd) and polarization (TE or TM) of SH modes. Here the odevity means the symmetry of the SH field in polar direction and is in terms of the axis of $\theta = \pi/2$.

pump polarization	SH properties with g_{SB}			SH properties with g_{B}	
	g_{sd}	$g_{\mathrm{s,var}}$	$g_{\mathrm{s,long}}$	g_{b1}	g_{b2}
TE	even, TM	even, TM	even, TM	odd, TE	odd, TE
TM	even, TM or TE	even, TM	even, TM	even, TM	even, TM

The SH power under TM polarized pumps is measured in the experiment, shown in Supplementary Figure **S4**. Compared with Figure 3b in the main text, it is found that SH power output with TM excitation is statistically one order of magnitude larger than that with TE excitation. This is because (*i*) TM pump excites both the symmetry-breaking effect and the pure bulk effect while TE pump only excites either of them; (*ii*) The effective surface susceptibility component related to TM pump is about one order of magnitude larger than that related to TE pump [8].

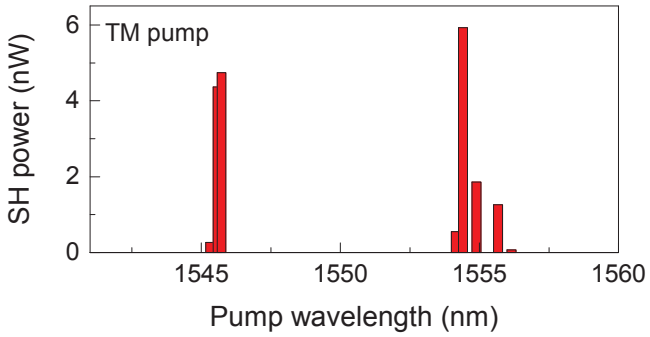

Supplementary Figure S4: **SH output under TM polarized pump.** SH power measured with TM pump polarization, in the pump wavelength ranging from 1541 nm to 1560 nm.

D. Comparison with conventional surface nonlinear optics

The identification of the symmetry-breaking-induced and pure bulk responses in a WGM cavity is intuitively elusive compared with the case in conventional surface nonlinear optics with plane waves. The main reason is that what we identified is the symmetry-breaking-induced nonlinearity at the surface, instead of the conventional surface nonlinearity. To make it clearer, we summarize the main differences between the conventional surface nonlinear optics and the surface symmetry-breaking-induced nonlinearity in WGM microcavities, as shown in Supplementary Table **S2**. It is found that the field distribution of WGMs and the collinear wave vectors are the key points to realize the identification. In the conventional situation, both surface and bulk nonlinear responses are present, and the usual approach is to extract the individual contribution by varying the operating parameters. However, in our case, the generated SH can be either from g_{SB} [contribution (*i*)-(*iii*)] or g_{SB} [contribution (*iv*)], but never the combination of

Supplementary Table S2: Comparison of the conventional surface nonlinear optics and the surface symmetry-breaking-induced nonlinearity in a WGM microcavity.

System	Conventional surface nonlinear optics	Whispering-gallery-mode microcavity
Schematic sketch	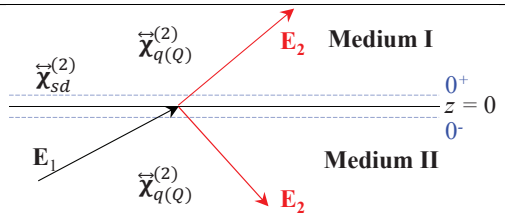	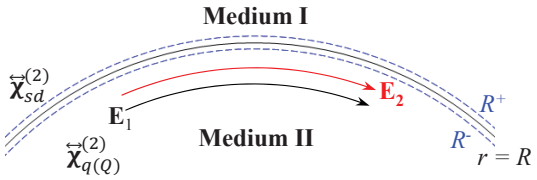
Wave form	Plane wave or Gaussian beam	Whispering gallery mode
Wave vectors	With components perpendicular to the surface	Parallel to the surface [ratio of the azimuthal and radial components is over 10^{13} (10^{14}) at 1550 nm (775 nm) band]
Spatial distribution	Non-uniform distribution only in propagating direction	Non-uniform distribution in all directions, with spherical symmetry
Phase matching	Not required	Required
Origins of SH	(*i*) An ED contribution from the surface layer. (*ii*) An EQ contribution from the rapid field variation at the interface. (*iii*) An EQ contribution from the bulk intrinsically inseparable from the surface ED contribution. (*iv*) An EQ contribution from the bulk.	(*i*) An ED contribution from the surface layer. (*ii*) An EQ contribution from the rapid field variation at the interface. (*iii*) An EQ contribution from a longitudinal source electric polarization at the surface. (*iv*) An EQ contribution from the bulk.
Otherwise	-	Non-degenerate TE and TM cavity modes

them, thus they can be identified. Additionally, the longitudinal electric-polarization contribution (*iii*) in a WGM microcavity is equivalent to the inseparable term (*iii*) in the conventional situation, which is evidently caused by the surface-induced symmetry-breaking in a WGM microcavity.

E. Measurement of SH mode field distributions

To identify the contributions of symmetry-breaking-induced and pure bulk nonlinearity, we measure the polar field distribution of the SH mode while scanning the signal fibre in the vertical direction. As shown in Figure 3a of the main text, the pump light with TE polarization is used to excite the WGM and generate SH light. Here the polarization of the pump is measured by a polarimeter (Thorlabs, PAX5710VIS-TXP). In the experiment, the distance between the coupling position and measurement point is made as short as possible (about 10 cm), and this part of the fibre is kept straight enough. In the measurement, the evident change is not found in the light polarization when light propagates in such a short and straight fibre. This result is confirmed by measuring the light polarization, (1) at the fibre output port and (2) of excited cavity modes, which show a good agreement. To obtain the polarizations of cavity modes, we adopt a widely-accepted characterization method [9, 10].

With the deterministic TE polarization of the pump, the signal fibre weakly coupled with the cavity is scanned in the vertical direction to measure the intensity distribution of SH modes. The major electric-field component of the cavity mode with TM polarization in a microsphere is given as

$$E_r = \frac{1}{\varepsilon_r\sqrt{\varepsilon_0}}\frac{l(l+1)c}{\omega r}\psi_l(\frac{\omega}{c}r)Y_l^m(\theta,\phi), \tag{S28}$$

$$E_\phi = \frac{1}{\varepsilon_r\sqrt{\varepsilon_0}}\frac{c}{\omega r}\frac{im}{\sin\theta}\frac{\mathrm{d}}{\mathrm{d}r}[r\psi_l(\frac{\omega}{c}r)]Y_l^m(\theta,\phi). \tag{S29}$$

The analytical intensity of the electric field along the red dashed line and the blue dotted curve in Supplementary Figure S5a can be derived from equations S28 - S29, as shown in Supplementary Figure S5b and Supplementary Figure S5c, respectively. Thus, the electric field on the red line at an certain vertical position z can be mapped to

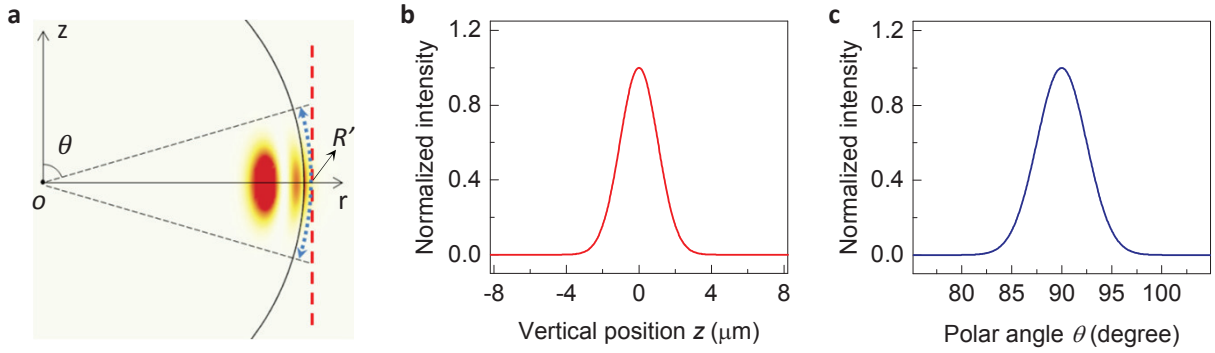

Supplementary Figure S5: **Method to map the electric field intensity onto the polar direction. a,** Schematic of the electric field distribution of an SH mode in a vertical plane. The red dashed line denotes the actual scan direction in the experiment, and the blue dotted curve stands for the corresponding polar direction. The polar angle (θ) is derived from the geometric relation: θ=arctan(R'/z), where R' is the radius of the curve and z is the vertical position. **b,** The normalized intensity of the electric field along the vertical direction [red dashed line in (**a**)]. **c,** The normalized intensity of the electric field along the polar direction [blue dotted curve in (**a**)].

the position on the blue curve with the polar angle of θ=arctan(R'/z).

[1] Guyot-Sionnest, P., Shen, Y. R. Bulk contribution in surface second-harmonic generation. *Phys. Rev. B* **38**, 7985 (1988).
[2] Shen, Y. R. Basic theory for surface sum-frequency generation. In *Fundamentals of sum-frequency spectroscopy*, chap. 3 (Cambridge University Press, 2016).
[3] Carmon, T., Yang, L. & Vahala, K. J. Dynamical thermal behavior and thermal self-stability of microcavities. *Opt. Express* **12**, 4742-4750 (2004).
[4] Fomin, A. E., Gorodetsky, M. L., Grudinin, I. S. & Ilchenko, V. S. Nonstationary nonlinear effects in optical microspheres. *J. Opt. Soc. Am. B* **22**, 459-465 (2005).
[5] Ghosh, G., Endo, M. & Iwasaki, T. Temperature-dependent sellmeier coecients and chromatic dispersions for some optical fiber glasses. *J. Lightwave Technol.* **12**, 1338-1342 (1994).
[6] Carmon, T. & Vahala, K. J. Visible continuous emission from a silica microphotonic device by third-harmonic generation. *Nat. Phys.* **3**, 430-435 (2007).
[7] Heinz, T. F. Second-order nonlinear optical effects at surfaces and interfaces. In Ponath, H.-E. & Stegeman, G. I. (eds.) *Nonlinear surface electromagnetic phenomena*, chap. 5 (Elsevier, Amsterdam, 1991).
[8] Rodriguez, F. J., Wang, F. X. & Kauranen, M. Calibration of the second-order nonlinear optical susceptibility of surface and bulk of glass. *Opt. Express* **16**, 8704-8710 (2008).
[9] Murib, M. S., Yüce, E., Gürlü, O. & Serpengüzel, A. Polarization behavior of elastic scattering from a silicon microsphere coupled to an optical fiber. *Photonics Res.* **2**, 45-50 (2014).
[10] Zhang, N. *et al.* Far-field single nanoparticle detection and sizing. *Optica* **4**, 1151-1156 (2017).